

Surface shear rheology of hydrophobin adsorption layers: laws of viscoelastic behaviour with applications to long-term foam stability

Krassimir D. Danov,^a Gergana M. Radulova,^a Peter A. Kralchevsky,^a Konstantin Golemanov^{ab} and Simeon D. Stoyanov^{bc}

Received 9th February 2012, Accepted 19th March 2012

DOI: 10.1039/c2fd20017a

The long-term stabilization of foams by proteins for food applications is related to the ability of proteins to form dense and mechanically strong adsorption layers that cover the bubbles in the foams. The hydrophobins represent a class of proteins that form adsorption layers of extraordinary high shear elasticity and mechanical strength, much higher than that of the common milk and egg proteins. Our investigation of pure and mixed (with added β -casein) hydrophobin layers revealed that their rheological behavior obeys a compound rheological model, which represents a combination of the Maxwell and Herschel–Bulkley laws. It is remarkable that the combined law is obeyed not only in the simplest regime of constant shear rate (angle ramp), but also in the regime of oscillatory shear strain. The surface shear elasticity and viscosity, E_{sh} and η_{sh} , are determined as functions of the shear rate by processing the data for the storage and loss moduli, G' and G'' . At greater strain amplitudes, the spectrum of the stress contains not only the first Fourier mode, but also the third one. The method is extended to this non-linear regime, where the rheological parameters are determined by theoretical fit of the experimental Lissajous plot. The addition of β -casein to the hydrophobin leads to softer adsorption layers, as indicated by their lower shear elasticity and viscosity. The developed approach to the rheological characterization of interfacial layers allows optimization and control of the performance of mixed protein adsorption layers with applications in food foams.

1. Introduction

The foams are thermodynamically unstable systems, which spontaneously decompose with time due to breakage of the liquid films intervening between the bubbles and due to the phenomenon Ostwald ripening (foam disproportionation).¹ These destructive processes, if not completely arrested, can be considerably slowed down, so that the foam could be considered stable in the time-scale of its practical applications. One of the strategies to stabilize foams, including foams in structured foods, is to “solidify” the bubble surfaces by covering them with a viscoelastic adsorption layer, which enhances the foam longevity at least in three aspects. First, the immobilization of the air/water interface slows down the film and foam drainage.^{2–5} Second, the stability of the foam films is strongly enhanced, and their

^aDepartment of Chemical Engineering, Faculty of Chemistry, Sofia University, 1164 Sofia, Bulgaria

^bUnilever Research & Development, 3133AT Vlaardingen, The Netherlands

^cLaboratory of Physical Chemistry and Colloid Science, Wageningen University, 6703 HB Wageningen, The Netherlands

permeability to gas transfer is considerably reduced. Third, the produced bubbles are considerably smaller and the foam viscoelasticity is markedly enhanced, which is important for the properties of many consumer products.^{6–8} In the case of foams and emulsions in the food industry, the main substances that are used to enhance the interfacial rheology are proteins, which form dense and elastic layers at the surfaces of gas bubbles and emulsion drops. The interfacial rheology of protein adsorption layers has been intensively studied in relation to the properties of protein-stabilized foams,^{9–11} emulsions,^{12–16} and mixed systems such as proteins with lipids,^{17,18} and proteins with surfactants.^{19–22} Detailed information on the investigated systems, experimental techniques and theoretical models can be found in review articles on interfacial shear rheology.^{22–27}

Recently, it was established that the hydrophobins are very promising stabilizers of foams^{9–11} and emulsions.^{28–30} They represent a class of proteins that are contained in filamentous fungi, including the common button mushroom.³¹ The hydrophobins are relatively small proteins, whose structure is stabilized by several disulfide bridges, so that they do not undergo structural changes upon adsorption at interfaces.^{31,32} The most remarkable property of the hydrophobins is that their adsorption layers at the air/water interface exhibit a considerable shear elasticity, which is higher than that of other investigated proteins.^{11,33} The adsorption layers from hydrophobins solidify soon after their formation.^{33,34} In applications, the hydrophobins can be used in mixtures with other proteins and/or surfactants,^{35,36} which can modify their foam-stabilizing effect. For this reason, it is important to quantify and compare the surface rheological properties of adsorption layers of hydrophobins and their mixtures with other amphiphiles.

In the experiment, rotational surface rheometers in oscillatory regime are often used, which give the phenomenological surface storage and loss moduli, G' and G'' as functions of the frequency and time.^{9–11} If the viscoelastic layer complies with the Kelvin law, then G' and G'' characterize, respectively, the elastic and viscous properties of the adsorption layer. The oscillatory regime does not give direct information on the applicability of the Kelvin or Maxwell model to a given system. However, an adsorption layer can be characterized with shear elasticity and viscosity, E_{sh} and η_{sh} , only in the framework of an adequate rheological model.

In a recent study,³⁶ we investigated the surface shear rheology of hydrophobin adsorption layers by a rotational rheometer in angle-ramp regime (increase of the rotation angle at a constant angular velocity). The results showed that the rheological behavior of the system complies with a combined Maxwell–Herschel–Bulkley law. From a physical viewpoint, if a rheological law is obeyed by a given continuous medium in a given kinetic regime, it should be obeyed by the same medium also in all other kinetic regimes. Our main goal in the present study is to investigate whether the combined Maxwell–Herschel–Bulkley model can also describe experimental data obtained in the oscillatory regime. This includes derivation of expressions for calculating the surface shear elasticity and viscosity, E_{sh} and η_{sh} , from the experimentally determined phenomenological moduli G' and G'' , and verification of whether the same E_{sh} and η_{sh} are obtained in the angle-ramp and oscillatory regimes. In this way, the adequacy of the used model will be confirmed.

For this goal, we carried out experiments with hydrophobin and mixed, hydrophobin + β -casein adsorption layers, which are described in Sections 2 and 3. Further, the combined Maxwell–Herschel–Bulkley model was applied to interpret the data and to determine E_{sh} and η_{sh} as functions of the shear-rate amplitude (Section 4). This analysis was carried out in the regime of not-too-large amplitudes, at which the rheological response of the system is quasi-linear, *i.e.* the stress oscillated with the basic frequency (that of the applied sinusoidal strain), the higher-order Fourier modes in the strain being negligible. However, the Herschel–Bulkley law is nonlinear, and at greater amplitudes the higher Fourier modes give non-negligible contributions to the stress, so that we are dealing also with the case of a nonlinear rheological response. The latter case is considered in Section 5. At sufficiently large

frequencies, the viscoelastic network of protein molecules at the interface can be broken as indicated by the Lissajous plots. The approach developed here for the investigation of hydrophobin adsorption layers is applicable also to any other viscoelastic interfacial layers.

2. Materials and methods

The used protein HFBII represents a class II hydrophobin.^{31,32} It was isolated from the fungus *Trichoderma reesei* following a procedure described elsewhere.³³ A stock solution of concentration 0.1 wt% was prepared. Before each experiment, this solution was sonicated in an ultrasound bath for 5 min to break-up the protein aggregates. Then, the necessary portion of the stock solution was diluted to 0.005 wt%.

The used β -casein from bovine milk, cat. No: C6905 by electrophoresis (assay >98%) was a product of Sigma. Mixed protein solutions were prepared with 0.005 wt% HFBII and 0.03 wt% β -casein. In view of the molecular masses of HFBII (7.2 kDa) and β -casein (24 kDa), the molar ratio β -casein/HFBII in the used solutions was 1.8.

Just before the rheological measurements, the working solution was sonicated again to break-up any newly formed protein aggregates. All solutions were prepared with deionized water of specific resistivity 18.2 M Ω -cm (Milli-Q purification system, Millipore, USA). In all experiments, the working temperature was 25 °C.

The surface shear rheology of the protein adsorption layers at the air/water interface was investigated by the rotational rheometer Bohlin Gemini, Malvern UK. This rheometer is equipped with a bi-conical tool for surface shear rheology measurements. The bi-conical tool is placed in a working cell, where the investigated solution is poured up to the edge of the tool. The outer radius of the bi-cone is $R_1 = 2.81$ cm; the inner radius of the wall of the cylindrical cell is $R_2 = 3.00$ cm, and the distance between them is $\Delta R = 0.19$ cm. The latter represents the width of the ring-shaped protein adsorption layer that is subjected to shear deformation.

Before each run, the solution in the experimental cell was replaced with a new portion. After loading the solution, we waited for 5 min before the start of the rheological measurements. This period of time is needed for the formation and consolidation of the adsorption layer. In general, the rheological properties of the protein adsorption layers vary with the surface age.^{13,15,19,37,38} For this reason, in our experiments the aging time was the same, 5 min in all runs. A similar aging time has been used also by other authors.¹⁵

Experiments in two different regimes have been carried out. First, in the *angle-ramp regime* the bi-conical tool rotates with a fixed angular velocity, $\dot{\theta}$, and the increase of the torque, τ , is recorded as a function of time, t . Second, in the *oscillatory regime* the rotation angle θ oscillates and the corresponding periodic variations in the torque τ are registered. Each experiment was repeated at least six times to be sure that the results are reproducible. The direct measurements with pure water showed that at the used low angular velocities ($\dot{\theta} \leq 0.132$ rad s⁻¹), no effect of the viscosity of the bulk aqueous phase is registered. In other words, the measured torque is completely due to the viscoelastic adsorption layer.

The primary data for $\theta(t)$ and $\tau(t)$ recorded by the apparatus have been used for further processing and interpretation. The values of the surface shear stress, τ_{sh} , were calculated from the measured torque, τ , as follows:^{15,39}

$$\tau_{\text{sh}} = g_{\text{r}} \tau, \quad g_{\text{r}} \equiv \frac{1}{4\pi} \left(\frac{1}{R_1^2} - \frac{1}{R_2^2} \right) \quad (1)$$

Here, g_{r} is a geometric factor; with $R_1 = 2.81$ cm and $R_2 = 3.00$ cm, eqn (1) gives $g_{\text{r}} = 12.36$ rad m⁻². Eqn (1) is applicable to surface layers of arbitrary viscoelastic behavior in the case of narrow gap, *i.e.* $(R_2 - R_1)/R_1 \leq 0.1$. In our case the latter ratio is 0.0676.

The adsorption layers of β -casein alone (even at a relatively high concentration of 0.17 wt%) gives a very weak rheological response, which is below the sensitivity threshold of the used apparatus—the registered torque τ is practically zero. Nonzero τ has been measured only in the presence of hydrophobin.

3. Experimental results

3.1. Solutions of 0.005 wt% HFBII

As mentioned above, in the oscillatory regime the rotation angle θ oscillates and the corresponding periodic variations in the torque τ are registered. First, we verified whether the $\theta(t)$ dependence generated by the apparatus is perfectly harmonic. For this goal, the experimental dependence $\theta(t)$ was fitted with a sinusoid:

$$\theta(t) = \theta_a \sin(\omega t_e + \phi) \quad (2)$$

see Fig. 1. Here, θ_a is the amplitude of oscillations; $\omega = 2\pi\nu$ is the angular frequency and ν is the conventional frequency; ϕ is a phase-shift angle, and t_e is the experimental time, as registered by the apparatus. The fits of the experimental data for $\theta(t)$ with eqn (2) showed that the oscillations of θ are sinusoidal with a very high precision (regression coefficient of at least 0.99995). For each experiment, θ_a and ϕ have been determined from the fit. For the needs of the subsequent theoretical analysis, it is convenient to introduce the theoretical time, t , and the strain, γ , as follows:

$$t = t_e + \phi/\omega, \quad \gamma = \tan\theta \quad (3)$$

Because the angle θ is small in our experiments, we have $\gamma \approx \theta$ and amplitudes $\gamma_a \approx \theta_a$ within an accuracy of at least six significant digits. For this reason, hereafter we will use the notation γ for both strain (measured in %) and rotation angle (measured in radians); 1 mrad = 0.1%. Likewise, $\gamma_a = \theta_a$ will denote the strain amplitude, and $\dot{\gamma} = \dot{\theta}$ will be the rate of strain, which represents also the angular velocity and the shear rate.

In view of eqn (3), eqn (2) acquires the form:

$$\gamma(t) = \gamma_a \sin(\omega t) \quad (4)$$

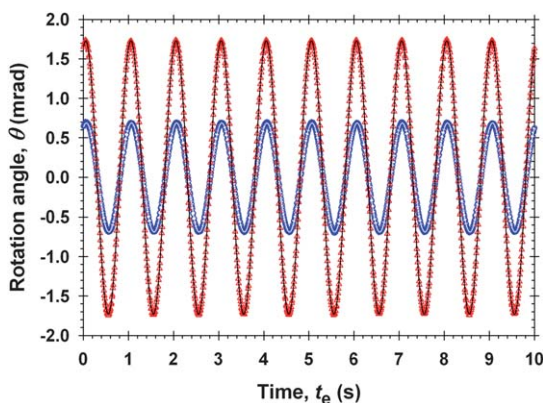


Fig. 1 Typical experimental dependence of the rotation angle, θ , on time, t_e , for 0.005 wt% HFBII at frequency $\nu = 1$ Hz, and at two different amplitudes: $\theta_a = 0.68$ and 1.74 mrad. The solid lines, which are fits by eqn (2), indicate that the strain is a perfect sinusoid.

For sufficiently small amplitudes, $\gamma_a \leq 5.235$ mrad, the registered torque τ (and Online shear stress $\tau_{\text{sh}} = g_f \tau$) also exhibits harmonic oscillations with phase shift, so that it can be expressed in the form:

$$\frac{\tau_{\text{sh}}}{\gamma_a} = G' \sin(\omega t) + G'' \cos(\omega t) \quad (5)$$

see Fig. 2; G' and G'' are the storage and loss moduli. Eqn (5) means that at small amplitudes the adsorption layer exhibits a quasi-linear rheological response (for a true linear response, the determined surface shear elasticity and viscosity have to be independent of the shear rate, $\dot{\gamma}$, whereas for a quasi-linear response they may depend on $\dot{\gamma}$; see Section 4.2 for details). Fig. 2a is typical for all measurements carried out at frequencies $\nu \leq 2$ Hz and amplitudes $\gamma_a \leq 5.235$ mrad. In contrast, Fig. 2b illustrates a special case at a higher frequency $\nu = 4$ Hz, at which the data for $\tau_{\text{sh}}(t)$ represent an experimental band, rather than a curve.

Our experiments show that at greater amplitudes, $\gamma_a \geq 10.5$ mrad, the periodical variations of τ_{sh} are not sinusoidal (Fig. 3), *i.e.* the adsorption layer exhibits

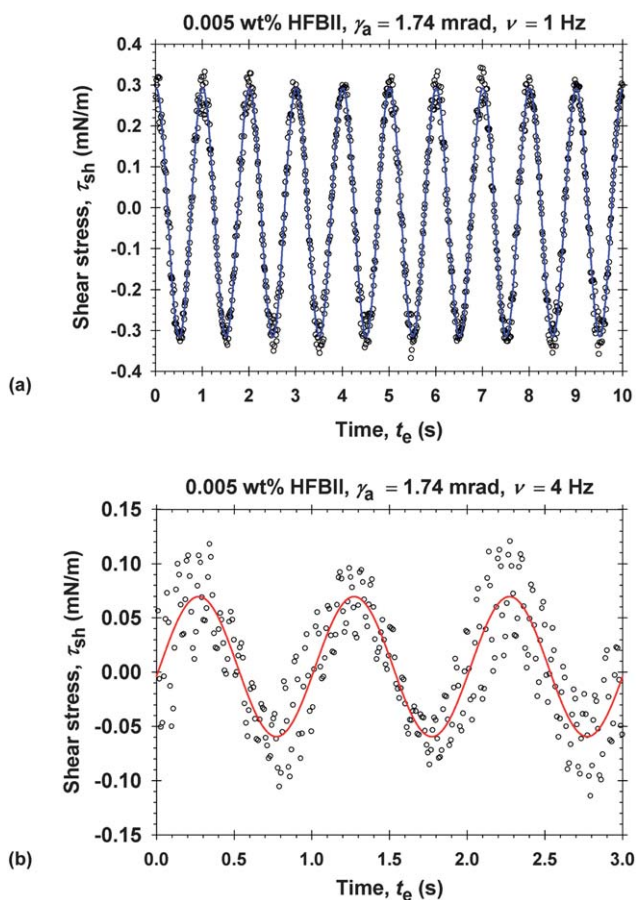


Fig. 2 Dependences of the measured stress, τ_{sh} , on time, t_e , for 0.005 HFBII, at strain amplitude $\gamma_a = 1.74$ mrad. The solid lines are the best fits with eqn (5). (a) The frequency is $\nu = 1$ Hz; this plot is typical for all measurements carried out at frequencies $\nu \leq 2$ Hz and amplitudes $\gamma_a \leq 5.235$ mrad. (b) The frequency is $\nu = 4$ Hz; the data for $\tau_{\text{sh}}(t)$ represent an experimental band, rather than an experimental curve.

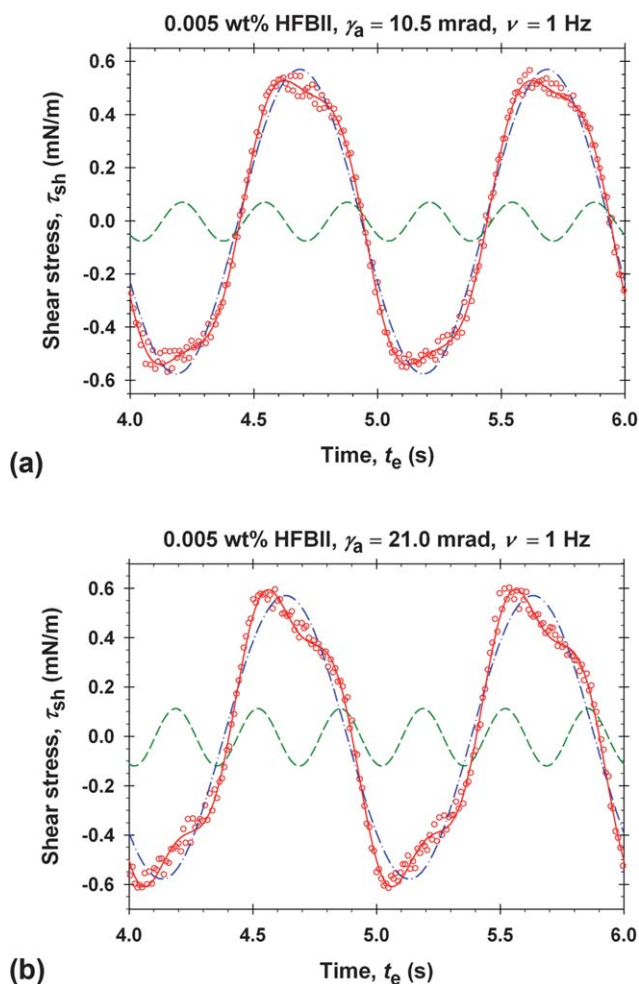


Fig. 3 Experimental dependences of the stress, τ_{sh} , vs. time, t_e , for 0.005 wt% HFBII in the case of nonlinear response; the frequency is $\nu = 1$ Hz; the strain amplitudes are (a) $\gamma_a = 10.5$ mrad; (b) $\gamma_a = 20.1$ mrad. The points are experimental data; the solid lines represent the best fit by eqn (6); the dash-dot and dashed lines are, respectively, the first and third Fourier modes.

a nonlinear rheological response. In such a case, instead of eqn (5), we have a Fourier series:

$$\frac{\tau_{sh}}{\gamma_a} = \sum_{k=1,3,5,\dots} [G'_k \sin(k\omega t) + G''_k \cos(k\omega t)] \quad (6)$$

It can be proven theoretically⁴⁰ that the Fourier expansion, eqn (6), can contain only odd modes ($k = 1, 3, 5, \dots$). This follows from the circumstance that rotations clockwise and anticlockwise are mechanically equivalent. For the data in Fig. 3, only the first two odd modes ($k = 1, 3$) are significant. The solid line in Fig. 3 shows the fit with eqn (6), whereas the dashed lines show the separate modes with $k = 1$ and 3. The values of the coefficients in eqn (6) determined from the fits of the data in Fig. 3 are given in Table 1, where the errors reflect the accuracy of the measurements,

Table 1 The storage and loss moduli, G'_k and G''_k , $k = 1, 3$, determined from the data in [Fig. 3](#) Online

γ_a (mrad)	First Fourier mode		Third Fourier mode	
	G'_1 (mN m ⁻¹)	G''_1 (mN m ⁻¹)	G'_3 (mN m ⁻¹)	G''_3 (mN m ⁻¹)
10.50	33.0 ± 0.3	43.4 ± 0.4	-4.65 ± 0.06	5.20 ± 0.07
20.99	5.73 ± 0.06	26.8 ± 0.3	-5.52 ± 0.06	0.55 ± 0.07

rather than their reproducibility. In general, the experiment indicates that the storage and loss moduli in eqn (6) depend on both amplitude γ_a and frequency ν :

$$G'_k = G'_k(\gamma_a, \nu), G''_k = G''_k(\gamma_a, \nu), k = 1, 3, 5, \dots \quad (7)$$

It is useful to plot the experimental data also in the form of Lissajous curves representing the stress $\tau_{sh}(t)$ vs. the strain $\gamma(t)$,⁴⁰ see Fig. 4. In the case of quasi-linear response ($\gamma_a \leq 5.23$ mrad), the Lissajous curves are ellipses, whereas in the case of nonlinear response ($\gamma_a = 10.5$ and 21.0 mrad), they look like curvilinear parallelograms of width that increases with the rise in γ_a . The Lissajous plots can be useful in several aspects.⁴⁰ First, by plotting the raw data for $\tau_{sh}(t)$ vs. $\gamma(t)$, the experimentalist can immediately verify whether the rheological response of the system is linear or nonlinear (ellipse vs. parallelogram). Second, if the Lissajous curves are wider than an ellipse (in nonlinear regime), as in Fig. 4, this indicates shear thinning, whereas a Lissajous curve that is concave with respect to an ellipse indicates shear thickening.⁴⁰ Last but not least, as demonstrated in Section 5 the parameters of the rheological model can be determined by a fit of the Lissajous curve without using a Fourier analysis.

In the oscillatory experiments with the rotational rheometer, there are two mechanical degrees of freedom: to vary the amplitude γ_a at a fixed frequency ν , and to vary ν at a fixed γ_a ; see also eqn (7). Fig. 5a presents the dependences of G'_1 and G''_1 on γ_a at $\nu = 1$ Hz. The data show that G'_1 decreases with the rise of the amplitude γ_a , whereas G''_1 initially increases until reaching G''_1 , and then exhibits a tendency to decrease.

Fig. 5b presents the dependences of G'_1 and G''_1 on the frequency ν at amplitude $\gamma_a = 1.74$ mrad. Initially, G'_1 increases with the rise in ν , but at the highest

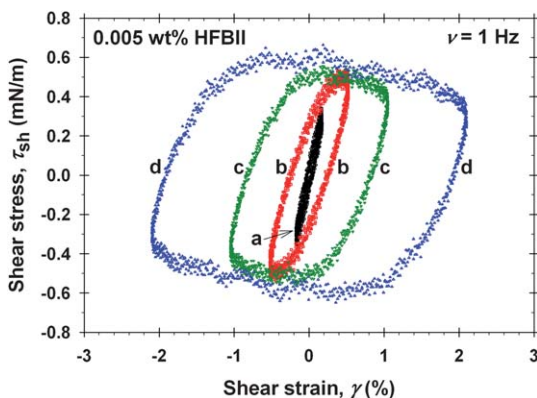


Fig. 4 Lissajous plots of the stress, $\tau_{sh}(t)$ vs. the strain, $\gamma(t)$, for 0.005 wt% HFBII at frequency $\nu = 1$ Hz, and at four different values of the strain amplitude, γ_a : (a) 1.74 mrad; (b) 5.23 mrad; (c) 10.5 mrad, and (d) 21.0 mrad.

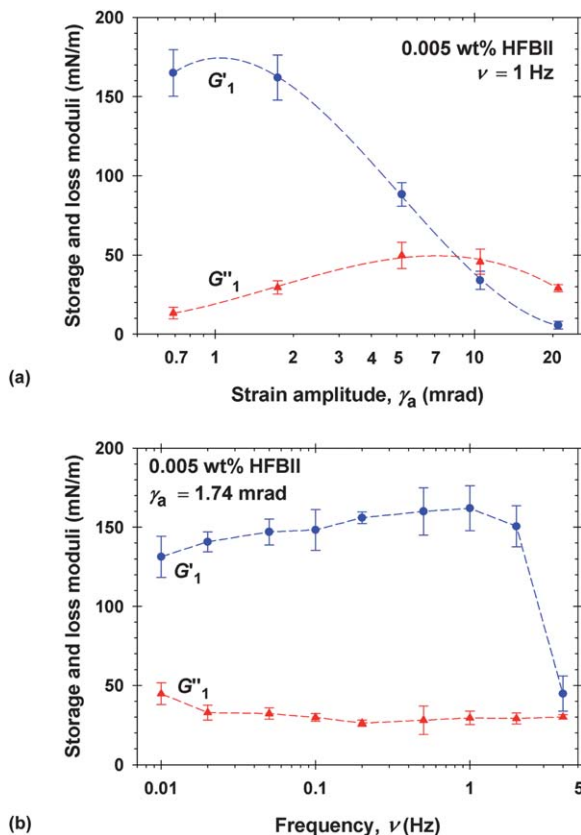


Fig. 5 Dependence of the storage and loss moduli, G'_1 and G''_1 (a) on the strain amplitude, γ_a , at fixed frequency, $\nu = 1$ Hz; (b) on the frequency, ν , at fixed strain amplitude, $\gamma_a = 1.74$ mrad. The data are for the adsorption layer at the surface of 0.005 wt% HFBII solution. Each point is the average value from 12 experiments. The dashed lines are guides to the eye.

investigated frequency it quickly decreases. In contrast, G''_1 initially slightly decreases, and then it levels off at the higher values of ν . Note that the highest investigated frequency is $\nu = 4$ Hz, which corresponds to the graph in Fig. 2b.

In Fig. 5a and b, every experimental point is an average of twelve independent experiments. Each of them is carried out by pouring a new portion of the investigated solution in the experimental cell of the rheometer. The experimental errors shown in Fig. 5a and b (unlike those in Table 1) represent the reproducibility (rather than the accuracy) of the rheological measurements, characterized by the standard deviation. As a rule, the accuracy of these measurements is much better than their reproducibility. An exclusion is observed at the highest frequency in Fig. 5b, $\nu = 4$ Hz, which corresponds to the graph in Fig. 2b. In this special case (which probably represents a broken viscoelastic layer; see Section 5) the data for $\tau_{sh}(t)$ are rather scattered, but they can be fitted well with a sinusoid (Fig. 2b). Interestingly, this sinusoid is well reproducible (the experiment was repeated 24 times), which is reflected by the relatively small error bars in Fig. 5b at $\nu = 4$ Hz.

3.2. Solutions of 0.005 wt% HFBII and 0.03 wt% β -casein

As mentioned above, one of our goals is to give a self-consistent interpretation of data obtained in oscillatory and angle-ramp regimes by the same rheological model. Data in angle-ramp regime have been reported in our previous study,³⁶ for both

HFBII and mixed HFBII + β -casein solutions. In the measurements reported [here](#), [Online](#) we used a new sample of β -casein, which turned out to give a slightly different rheological behavior of the mixed layers—a lower elasticity in comparison with the β -casein sample used in ref. 36. Here the data in both the angle-ramp and oscillatory regime have been obtained with the new sample of β -casein.

Fig. 6 shows experimental curves for the variation of the stress, τ_{sh} , with the increase of the rotation angle, γ , in the *angle-ramp* regime. Each curve corresponds to a fixed shear rate, $\dot{\gamma} = \text{const}$. The dependence $\tau_{\text{sh}}(\gamma)$ exhibits a clear tendency to level off at the larger γ . In addition, τ_{sh} increases with the rise of the shear rate, $\dot{\gamma}$.

Fig. 7 presents data for the storage and loss moduli G'_1 and G''_1 as functions of the frequency, ν , in *oscillatory* regime at fixed amplitude $\gamma_a = 1.74$ mrad ($\gamma_a = 0.174\%$). At this amplitude, the rheological response of the adsorption layer is quasi-linear, *i.e.* the effect of the higher-order harmonics (G'_3 and G''_3) is negligible. The comparison of Fig. 5b and 7 indicates that the addition of β -casein leads to lowering of both G'_1 and G''_1 . Moreover, the decrease of G'_1 with the rise of ν begins at lower frequencies.

4. Theoretical models vs. experimental results

As demonstrated below, the obtained experimental data comply with a compound rheological model, which combines the Maxwell model with a modified Herschel–Bulkley law. We begin with a brief overview and discussion on the applicability of simpler models.

4.1. Models with constant E_{sh} and η_{sh}

The *Kelvin model*, known also as Kelvin–Voigt model,^{41,42} is characterized with a parallel connection of an elastic and a viscous element (Fig. 8a). The latter two elements are characterized by the conventional stress–strain relationships:

$$\tau_{\text{sh,e}} = E_{\text{sh}}\gamma, \quad \tau_{\text{sh,v}} = \eta_{\text{sh}}\dot{\gamma} \quad (8)$$

where $\tau_{\text{sh,e}}$ and $\tau_{\text{sh,v}}$ are, respectively, the elastic and viscous stresses; E_{sh} and η_{sh} are the coefficients of surface shear elasticity and viscosity and (as usual) γ and $\dot{\gamma}$ are the shear strain and rate-of-strain. Note that in the conventional Kelvin model, E_{sh} and η_{sh} are constants independent of time, t .

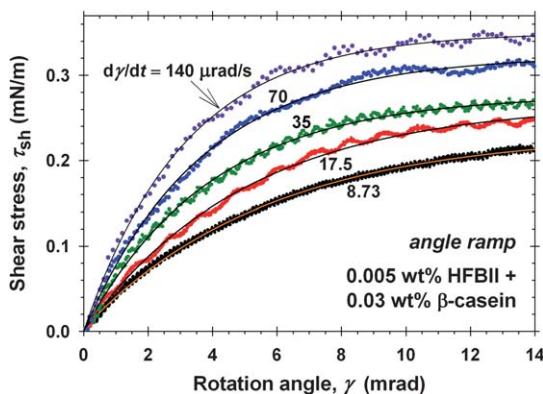


Fig. 6 Experimental data obtained in angle-ramp regime for adsorption layers at the surface of 0.005 wt% HFBII + 0.03 wt% β -casein solutions: Plots of the stress, τ_{sh} , vs. the rotation angle, γ , at three different fixed angular velocities: $\dot{\gamma} = 8.73, 17.5, 35, 70$ and $140 \mu\text{rad s}^{-1}$; the time is expressed as $t = \gamma/\dot{\gamma}$. The solid lines are fits by the Maxwell model, eqn (15).

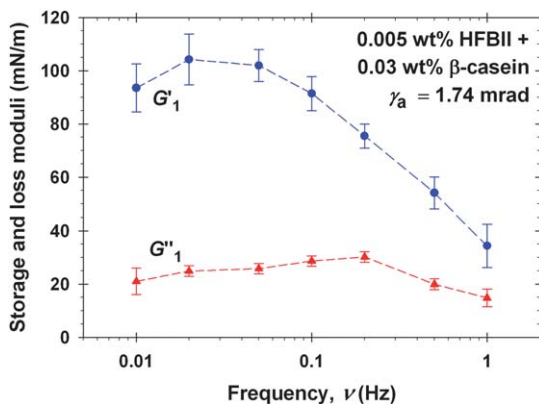


Fig. 7 Dependence of the storage and loss moduli, G'_1 and G''_1 on the frequency, ν , at fixed strain amplitude, $\gamma_a = 1.74$ mrad. The data are for the adsorption layer at the surface of 0.005 wt% HFBII + 0.03 wt% β -casein solution. Each point is the average value from 12 experiments. The dashed lines are guides to the eye.

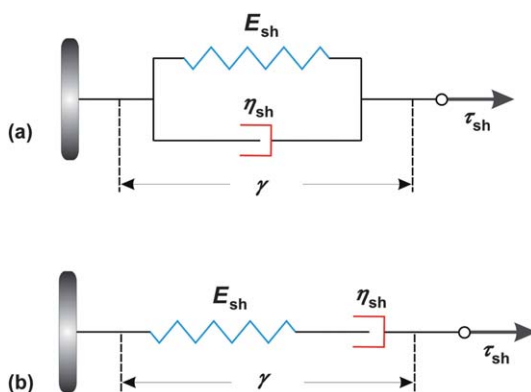


Fig. 8 Sketch of the two basic compound models of viscoelastic behavior composed of an elastic element (spring) of elasticity E_{sh} , and a viscous element (dash-pot) of viscosity η_{sh} . (a) The Kelvin model: parallel connection. (b) The Maxwell model: consecutive connection. τ_{sh} is the applied stress; γ is the total strain.

In the Kelvin model (Fig. 8a), the strain is the same for the two elements, whereas the total stress equals the sum of the elastic and viscous stresses:

$$\tau_{sh} = E_{sh}\gamma + \eta_{sh}\dot{\gamma} \quad (9)$$

Substituting γ and τ_{sh} from eqn (4) and (5) into eqn (9), we obtain:

$$G' = E_{sh}, G'' = \eta_{sh}\omega \quad (10)$$

In other words, if a given body obeys the Kelvin model, then the storage modulus G' is constant and equal to the elasticity, whereas the loss modulus G'' increases linearly with the frequency, $\omega = 2\pi\nu$, both of them being independent of the amplitude γ_a .

As seen in Fig. 5 and 7, our experimental system does not obey the Kelvin law (G' and G'' depend on γ_a , and G'' does not increase linearly with ν). Moreover, in the

angle-ramp regime ($\dot{\gamma} = \text{const.}$) eqn (9) gives $\tau_{\text{sh}} = E_{\text{sh}} \dot{\gamma} t + \text{const.}$, *i.e.* the stress τ_{sh} to linearly increase with time, which cannot explain the experimentally observed tendency of τ_{sh} to level off (Fig. 6).

The Maxwell model,⁴³ is characterized with a consecutive connection of an elastic and a viscous element (Fig. 8b). Hence, the stress, τ_{sh} , is the same for the two elements, whereas the total rate-of-strain equals the sum of the elastic and viscous rates-of-strain:

$$\frac{1}{E_{\text{sh}}} \frac{d\tau_{\text{sh}}}{dt} + \frac{\tau_{\text{sh}}}{\eta_{\text{sh}}} = \dot{\gamma} \quad (11)$$

Substituting γ and τ_{sh} from eqn (4) and (5) into eqn (11) and setting equal the coefficients before the sine and cosine, we obtain:

$$G' = \frac{E_{\text{sh}}(\eta_{\text{sh}}\omega)^2}{E_{\text{sh}}^2 + (\eta_{\text{sh}}\omega)^2}, \quad G'' = \frac{E_{\text{sh}}^2\eta_{\text{sh}}\omega}{E_{\text{sh}}^2 + (\eta_{\text{sh}}\omega)^2} \quad (12)$$

The two relations in eqn (12) can be solved with respect to E_{sh} and η_{sh} :

$$E_{\text{sh}} = \frac{G'^2 + G''^2}{G'}, \quad \eta_{\text{sh}} = \frac{G'^2 + G''^2}{G''\omega} \quad (12a)$$

Eqn (12) implies that in the conventional Maxwell model (at constant E_{sh} and η_{sh}), G' and G'' depend on the frequency ω , but are independent of the amplitude, γ_{a} . The latter is in contradiction with our data in Fig. 5a.

Note that the rheological response of the system is characterized with a specific frequency ν_{ch} (or characteristic time $t_{\text{ch}} = 1/\nu_{\text{ch}}$) defined as follows:

$$\nu_{\text{ch}} \equiv \frac{G''}{G'} \omega = \frac{E_{\text{sh}}}{\eta_{\text{sh}}} \quad (13)$$

where eqn (12) has been used at the last step.

4.2. Generalization of the Maxwell model

In angle-ramp regime, the shear rate is constant, *i.e.* $\dot{\gamma} = \text{const.}$ Then, integrating eqn (11) along with the initial condition $\tau_{\text{sh}}|_{t=0} = 0$, we obtain:

$$\tau_{\text{sh}} = \eta_{\text{sh}}\dot{\gamma}[1 - \exp(-\nu_{\text{ch}}t)] \quad (14)$$

where the definition (13) has been also used. Because in angle-ramp regime $t = \gamma/\dot{\gamma}$, eqn (14) can be expressed also in the form:

$$\tau_{\text{sh}} = \eta_{\text{sh}}\dot{\gamma}[1 - \exp(-\nu_{\text{ch}}\gamma/\dot{\gamma})] \quad (15)$$

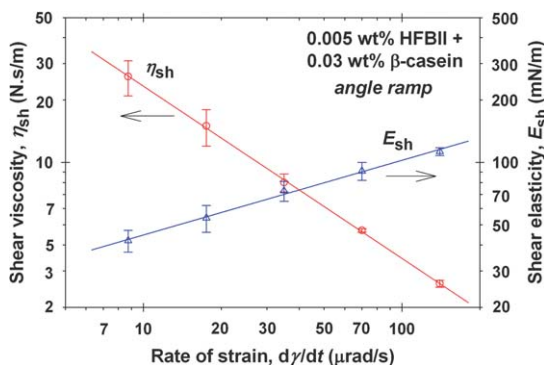
At each fixed angular velocity $\dot{\gamma}$ (angle-ramp regime), the experimental τ -vs.- γ curve excellently agrees with eqn (15). This is illustrated in Fig. 6, for the mixed system HFBII + β -casein. Similar results have been obtained for pure HFBII.³⁶ From the fits, the parameters η_{sh} and ν_{ch} have been determined. The results for η_{sh} and $E_{\text{sh}} = \nu_{\text{ch}}\eta_{\text{sh}}$ are listed in Table 2 and plotted in Fig. 9. The values in Table 2 are average from six experiments, and the errors of these values reflect the reproducibility of the experiments. (The errors of E_{sh} , η_{sh} and ν_{ch} determined from the errors of the parameters of each separate fit in Fig. 6 are much smaller.)

The Herschel–Bulkley law⁴⁴ reads:

$$\tau_{\text{sh}} = K\dot{\gamma}^n = \eta_{\text{sh}}\dot{\gamma} \Rightarrow \eta_{\text{sh}} = K\dot{\gamma}^{n-1} \quad (16)$$

Table 2 Parameters determined from the fit of the experimental curves in Fig. 6 with eqn (15) Online
0.005 wt% HFBII + 0.03 wt% β -casein; angle-ramp regime

$\dot{\gamma}$ ($\mu\text{rad s}^{-1}$)	E_{sh} (mN m^{-1})	η_{sh} (N.s/m)	ν_{ch} (10^{-3} Hz)
8.73	42 ± 5	26 ± 5	1.6 ± 0.3
17.5	54 ± 8	15 ± 3	3.5 ± 0.7
35.0	73 ± 8	8.0 ± 0.8	9.1 ± 0.8
70.0	91 ± 9	4.7 ± 0.1	19 ± 3
140.0	113 ± 5	2.6 ± 0.1	45 ± 4

**Fig. 9** Shear viscosity, η_{sh} , and elasticity, E_{sh} , vs. the rate of strain (the angular velocity) $\dot{\gamma}$: Plots of the data from Table 2 for 0.005 wt% HFBII + 0.03 wt% β -casein obtained in the angle-ramp regime in accordance with eqn (17). Each point is the average value from 6 experiments. The slopes of the linear regressions are given in Table 3.

where K is the consistency and n is the flow behavior index. At $n = 1$, the continuous medium behaves as a Newtonian fluid ($\eta_{\text{sh}} = \text{const.}$); for $n < 1$ and $n > 1$, the medium exhibits, respectively, shear thinning and thickening.

The data in Fig. 9 indicate that in the considered interval of shear rates η_{sh} , E_{sh} and ν_{ch} can be expressed as power functions:

$$\eta_{\text{sh}} = K|\dot{\gamma}|^{n-1}, E_{\text{sh}} = A|\dot{\gamma}|^p \quad (17)$$

$$\nu_{\text{ch}} = Q|\dot{\gamma}|^m \text{ (modified Herschel–Bulkley law)} \quad (18)$$

where A , K , Q , m , n and p are constant parameters ($m = p - n + 1$), see eqn (13). The modulus of $\dot{\gamma}$ was inserted in view of subsequent generalization to oscillatory regime, for which $\dot{\gamma}$ can be both positive and negative. Note that the elasticity and viscosity are independent of whether the rotation is clockwise or anticlockwise, so in general they must depend on $|\dot{\gamma}|$:⁴⁰

$$\eta_{\text{sh}} = \eta_{\text{sh}}(|\dot{\gamma}|), E_{\text{sh}} = E_{\text{sh}}(|\dot{\gamma}|) \quad (19)$$

In other words, η_{sh} and E_{sh} are even functions of $\dot{\gamma}$, which leads to the conclusion that the Fourier expansion, eqn (6) can contain only odd harmonics.⁴⁰

Thus, the experiments in angle-ramp regime imply that the rheological behavior of protein adsorption layers can be described by using the basic equation of the

4.3. Oscillatory regime with quasi-linear response

Here, it will be demonstrated that the combined Maxwell–Herschel–Bulkley model, based on eqn (11) and (18), describes also the rheological behavior of the investigated protein layers in oscillatory regime. In this regime, $\dot{\gamma} = \gamma_a \omega \cos(\omega t)$ is a periodic function of time (rather than constant as in the angle-ramp regime). In view of eqn (18) and (19), E_{sh} , η_{sh} and $\nu_{ch} = E_{sh}/\eta_{sh}$ are also periodic functions of time.

As discussed above, for small strain amplitudes (in our case, $\gamma_a \leq 5.235$ mrad; see Fig. 2) the investigated protein layers exhibit quasi-linear response, *i.e.* the higher-order harmonics have negligible amplitudes, so that the stress obeys eqn (5). Then, substituting eqn (4) and (5) into eqn (11), we derive:

$$(\nu_{ch} G'' + G') \cos(\omega t) + (\nu_{ch} G' - G'') \sin(\omega t) = E_{sh} \omega \cos(\omega t) \quad (20)$$

The multiplication of eqn (20) by $\sin(\omega t)$ and $\cos(\omega t)$, with a subsequent integration and some transformations, yields:

$$\langle \nu_{ch} \rangle \equiv \frac{G''}{G'} \omega = \frac{2}{\pi} \int_0^\pi \nu_{ch} \sin^2 \xi d\xi \quad (21)$$

$$G' + \frac{2G''}{\pi\omega} \int_0^\pi \nu_{ch} \cos^2 \xi d\xi = \frac{2}{\pi} \int_0^\pi E_{sh} \cos^2 \xi d\xi \quad (22)$$

$\xi \equiv \omega t$ is an integration variable. In view of eqn (13), the left-hand side of eqn (21) can be considered as an average characteristic frequency, $\langle \nu_{ch} \rangle$. If ν_{ch} is independent of time (as in the angle-ramp regime), then eqn (21) acquires the form $\langle \nu_{ch} \rangle = \nu_{ch}$, as it should be expected. If ν_{ch} and E_{sh} depend on time (as in the oscillatory regime), the two algebraic expressions in eqn (12a) are not valid; instead of them we have eqn (21) and (22).

In the case of oscillatory regime, we substitute $\nu_{ch}(\dot{\gamma})$ from eqn (18) with $\dot{\gamma} = \gamma_a \omega \cos(\xi)$ in the right-hand side of eqn (21). The integral can be solved and the result can be presented in the form:

$$\langle \nu_{ch} \rangle = Q \langle \dot{\gamma} \rangle^m \quad (23)$$

$$\langle \dot{\gamma} \rangle \equiv \mu \gamma_a \omega, \quad \mu \equiv \left[\frac{\Gamma(m/2 + 0.5)}{\pi^{1/2} \Gamma(m/2 + 2)} \right]^{1/m} \quad (24)$$

$\Gamma(x)$ is the gamma function. In analogy with eqn (18), eqn (23) expresses the mean characteristic frequency, $\langle \nu_{ch} \rangle$, as a power function of the mean shear rate, $\langle \dot{\gamma} \rangle$, defined by eqn (24).

Eqn (23) allows us to compare the experimental results obtained in angle-ramp and oscillatory regimes, see Fig. 10. In the *angle-ramp* regime, the characteristic frequency is calculated from the expression $\nu_{ch} = E_{sh}/\eta_{sh}$, where E_{sh} and η_{sh} are determined as adjustable parameters from fits of the data like those in Fig. 6. In Fig. 10, ν_{ch} is plotted vs. the shear rate $\dot{\gamma}$ in double logarithmic scale; m and Q are determined from the slope and intercept of the obtained linear dependence. The used data for 0.005 wt% HFBII + 0.03 wt% β -casein are these in Fig. 6 and Table 2, whereas the respective data for 0.005 wt% HFBII (without added β -casein) have been obtained in ref. 36 in the angle-ramp regime.

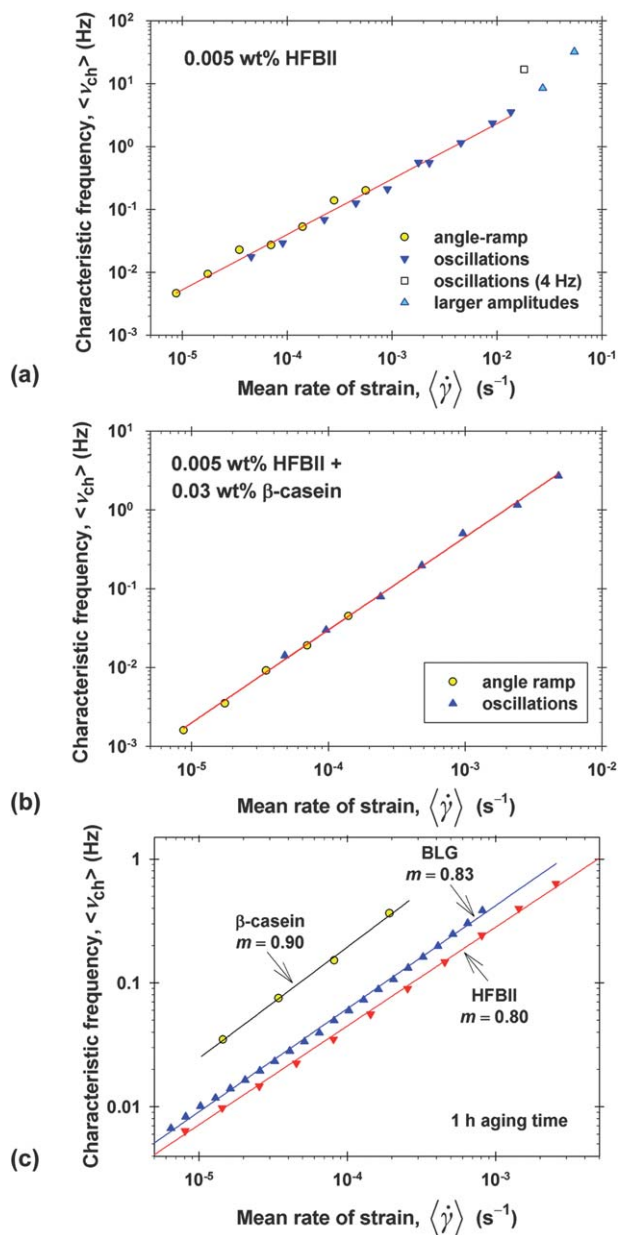


Fig. 10 Plots of the characteristic frequency of rheological response vs. the mean rate of strain. For the angle-ramp regime, the plot is $\nu_{ch} \equiv E_{sh}/\eta_{sh}$ vs. $\dot{\gamma}$. For the oscillatory regime, the respective mean quantities are plotted: $\langle \nu_{ch} \rangle \equiv \omega G''/G'$ vs. $\langle \dot{\gamma} \rangle$. The slope and intercept of the linear regression give m and Q ; see eqn (18) and (23). (a) Data for 0.005 wt% HFBII. (b) Data for 0.005 wt% HFBII + 0.03 wt% β -casein. (c) Comparison with literature data¹¹ for β -casein, β -lactoglobulin and HFBII from measured in the oscillatory regime.

The data points in the *oscillatory* regime (Fig. 10) were obtained in the following way. $\langle \nu_{ch} \rangle = \omega G''/G'$ was calculated from the experimental data in Fig. 5 and 7 ($G' = \tilde{G}'_1$, $G'' = \tilde{G}''_1$). Then, $\langle \nu_{ch} \rangle$ was plotted vs. $\gamma_{a\omega}$ in a double logarithmic scale; m and Q were determined from the slope and intercept of the obtained linear dependence. The values of m and Q obtained from the fits of the data in angle-ramp and

oscillatory regimes are very close, which confirms the applicability of the combined Maxwell–Herschel–Bulkley model to protein adsorption layers. View Article Online

The values of m and Q in Table 3 were obtained by a simultaneous fit of the data from the angle-ramp and oscillatory regime with the help of numerical minimization of the respective compound merit function. From the obtained value of m , we calculated also the coefficient μ in eqn (24) which is also given in Table 3. The values of n and p refer to the asymptotic region of sufficiently small $\dot{\gamma}$, where the power laws in eqn (17) are obeyed; see Fig. 9.

The three points in the upper-right corner of Fig. 10a correspond to oscillatory regime with nonlinear rheological response (greater amplitude or frequency of oscillations), at which the terms with $k = 3$ in eqn (6) are not negligible. In this case, the mean characteristic frequency is calculated from the first Fourier modes: $\langle \nu_{\text{ch}} \rangle = \omega G''/G'$. The respective points in Fig. 10a are close to the linear dependence that holds in the case of quasi-linear response, but still deviate from it.

As seen in Fig. 10b, the data for the adsorption layers at the surface of mixed solutions of HFBII and β -casein also comply with eqn (23) when plotted as ν_{ch} vs. $\langle \dot{\gamma} \rangle$. The results obtained in angle-ramp and oscillatory regimes are in excellent agreement.

Not only HFBII, but also other proteins form viscoelastic adsorption layers at the air/water interface. To check whether their behavior complies with eqn (23), in Fig. 10c we have plotted data for adsorption layers from β -casein, β -lactoglobulin (BLG) and HFBII obtained by rotational rheometer in oscillatory regime in Ref. 11. The original data¹¹ are in terms of G' and G'' , from which we calculated $\langle \nu_{\text{ch}} \rangle = \omega G''/G'$. Fig. 10c shows that the data for β -casein and BLG excellently agree with straight lines in accordance with eqn (23). The values of the exponent m are close, in the range 0.8–0.9, for all these proteins. In other words, the combined Maxwell–Herschel–Bulkley model is applicable not only to layers from hydrophobin, but also to viscoelastic adsorption layers from other proteins. In particular, the data for HFBII obtained here and in ref. 11 are in good agreement, with a small difference in the exponent: $m = 0.88$ (Fig. 10a) vs. $m = 0.80$ (Fig. 10c). (Smaller m corresponds to more rigid layer.) This difference can be attributed to the different surface ages of the adsorption layers (before the beginning of the rheological measurements): 5 min in our experiments vs. 1 h in ref. 11.

In general, the surface rheology of proteins varies with age. For proteins such as β -lactoglobulin and ovalbumin this effect is mostly due to conformational changes, which occur with the protein molecules after their adsorption. For the rigid hydrophobin molecules conformational changes are not expected, but the number of hydrophobin aggregates that adsorb below the protein adsorption layer is increasing with time, which can also lead to age effects.

4.4. Dependences of E_{sh} and η_{sh} on the rate of strain

The comparison of theory and experiment (Fig. 10) shows that the power dependence in eqn (18), viz. $\nu_{\text{ch}} = Q|\dot{\gamma}|^m$, is applicable in the whole region of quasi-linear response of the protein adsorption layer. However, the comparison with the experiment indicates that the power dependencies $\eta_{\text{sh}}(\dot{\gamma})$ and $E_{\text{sh}}(\dot{\gamma})$ in eqn (17) can be used only at sufficiently low shear rates. To find $\eta_{\text{sh}}(\dot{\gamma})$ and $E_{\text{sh}}(\dot{\gamma})$ in the whole region of quasi-linear response, we will employ eqn (22), which has not been used so far.

Table 3 Parameters in eqn (17)–(18) and (23)–(24) determined from fits of experimental data.^a

Solution	m	n	p	Q (s^{m-1})	μ
0.005 wt% HFBII	0.88	0.14	0.02	134	0.413
0.005 wt% HFBII + 0.03 wt% β -casein	1.18	0.17	0.35	1538	0.440

^a Note: The values of n and p refer to the asymptotic region of small shear rates; $m = p - n + 1$.

$$\langle E_{\text{sh}} \rangle \equiv \frac{2}{\pi} \int_0^{\pi} E_{\text{sh}} \cos^2 \xi \, d\xi \quad (25)$$

For $E_{\text{sh}} = \text{const.}$ Eqn (25) yields $\langle E_{\text{sh}} \rangle = E_{\text{sh}}$. Substituting ν_{ch} from eqn (18) into eqn (22), in view of eqn (25) we obtain:

$$\langle E_{\text{sh}} \rangle = G' + (m+1) \frac{G''}{\omega} Q \langle \dot{\gamma} \rangle^m = \frac{G'^2 + (m+1)G''^2}{G'} \quad (26)$$

where eqn (21) and (23) have been used at the last step. The combination of eqn (25) and (26) gives an integral equation for determining the function $E_{\text{sh}}(\xi)$. The problem can be solved by using an appropriate empirical expression for $E_{\text{sh}}(\dot{\gamma})$. To find such an expression, one can utilize the fact that the $E_{\text{sh}}(\dot{\gamma})$ dependence is similar to the dependence of $\langle E_{\text{sh}} \rangle$ on the amplitude $\gamma_a \omega$ (we recall that $\dot{\gamma} = \gamma_a \omega \cos(\omega t)$). The latter dependence can be calculated from eqn (26) using experimental data for G' and G'' , and the value of m that is known from the fit in Fig. 10 (see Table 3).

In this way, from the data for 0.005 wt% HFBII (without added β -casein), it was found that we can seek $E_{\text{sh}}(\dot{\gamma})$ in the form:

$$E_{\text{sh}} = a_0 \exp(a_1 |\dot{\gamma}| - a_2 |\dot{\gamma}|^2) \quad (27)$$

where $\dot{\gamma} = \gamma_a \omega \cos(\xi)$. The empirical parameters a_0 , a_1 and a_2 are to be determined from the fit of experimental data, as follows. The points in Fig. 11a are calculated from eqn (26), where the experimental values of G' and G'' from Fig. 5b are substituted. These points, expressing the experimental $\langle E_{\text{sh}} \rangle$, are fitted with the theoretical dependence of $\langle E_{\text{sh}} \rangle$ on $\gamma_a \omega$, which is obtained by substituting eqn (27) in the integrand of eqn (25). The parameter values determined from the fit (the dashed line in Fig. 11a) are:

$$a_0 = 160 \text{ mN m}^{-1}, a_1 = 15.3 \text{ s}, a_2 = 771 \text{ s}^2 \quad (28)$$

With the above parameter values, the dependence $E_{\text{sh}}(\dot{\gamma})$ is calculated from eqn (27) with $\dot{\gamma} \equiv \gamma_a \omega$; see the solid line in Fig. 11a. One sees that the curves representing E_{sh} and $\langle E_{\text{sh}} \rangle$ are really very close, the greatest differences appearing in the zone of larger variations of E_{sh} , as it could be expected in view of eqn (25). Finally, the dependence of viscosity on the shear rate is calculated using the relationship $\eta_{\text{sh}} = E_{\text{sh}}/\nu_{\text{ch}}$, where ν_{ch} is given by eqn (18) with $\dot{\gamma} \equiv \gamma_a \omega$.

In the case of 0.005 wt% HFBII + 0.03 wt% β -casein, the data suggest that we can seek $E_{\text{sh}}(\dot{\gamma})$ in the form:

$$E_{\text{sh}} = b_0 + b_1 \exp(-b_2 |\dot{\gamma}|) [1 - \exp(-b_3 |\dot{\gamma}|)] \quad (29)$$

where $\dot{\gamma} = \gamma_a \omega \cos(\xi)$. The empirical parameters b_0 , b_1 , b_2 and b_3 have been determined from the fit of the data in Fig. 11b in the following way. Two sets of experimental data have been simultaneously fitted. The first one includes the data for G' and G'' from Fig. 7 obtained in oscillatory regime, which are substituted in eqn (26) to find $\langle E_{\text{sh}} \rangle$ as a function of the rate-of-strain amplitude $\gamma_a \omega$; see the points in Fig. 11b. The second set consists of the data for E_{sh} vs. $\dot{\gamma}$ from Table 2 that have been obtained in an angle-ramp regime; see the inset in Fig. 11b. The theoretical curve in Fig. 11b was computed from eqn (25) along with eqn (29). The least squares method was applied to fit the data with a merit function that represents a sum of two merit functions corresponding to the sets of data obtained in

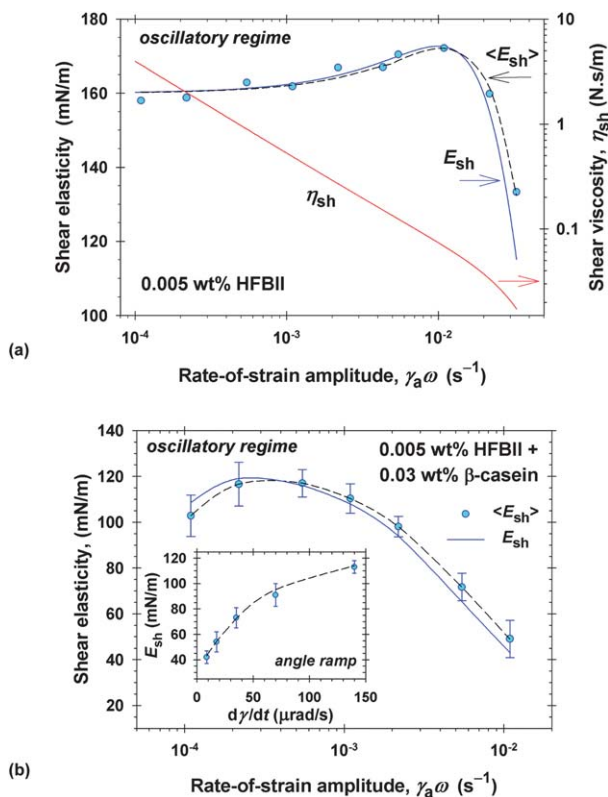


Fig. 11 Plots of shear elasticity vs. rate-of-strain amplitude. The points represent the mean elasticity (E_{sh}) calculated from eqn (26) using the experimental $G'(\gamma_a \omega)$ and $G''(\gamma_a \omega)$ dependences. The dashed lines represent the best fits with eqn (25), along with eqn (27) or (29). (a) Results for 0.005 wt% HFBI; E_{sh} is calculated from eqn (27) and (28) with $\dot{\gamma} = \gamma_a \omega$; then, $\eta_{sh} = E_{sh}/\nu_{ch}$. (b) Results for 0.005 wt% HFBI + 0.03 wt% β -casein; E_{sh} is calculated from eqn (29) and (30) with $\dot{\gamma} = \gamma_a \omega$; the inset shows data for E_{sh} obtained in angle-ramp regime, which are fitted simultaneously with the data for $\langle E_{sh} \rangle$ obtained in oscillatory regime.

angle-ramp and oscillatory regimes. From a statistical viewpoint, this is the most appropriate method, because the experimental error of the variables is correctly taken into account. Of course, it is possible to merge the data from the inset with the main curve in Fig. 11b by using an effective amplitude $\gamma_a \omega \equiv \dot{\gamma}/\mu$ along the horizontal axis for the data in angle-ramp regime; see eqn (24). The combined dependence, corresponding to eqn (29), is shown in Fig. 12a. The parameter values determined from the best fit are:

$$b_0 = 30 \text{ mN m}^{-1}, b_1 = 95 \text{ mN m}^{-1}, b_2 = 181 \text{ s}^{-1}, b_3 = 16978 \text{ s}^{-1} \quad (29a)$$

Fig. 12b shows the respective dependence of viscosity on the shear rate, which is calculated using the relationship $\eta_{sh} = E_{sh}/\nu_{ch}$, where ν_{ch} is given by eqn (18) with $\dot{\gamma} \equiv \gamma_a \omega$, and with m and Q from Table 3.

4.5. Summary and discussion

4.5.1. The combined Maxwell–Herschel–Bulkley model. As mentioned above, it is remarkable that the modified Herschel–Bulkley law in terms of ν_{ch} vs. $\dot{\gamma}$, eqn

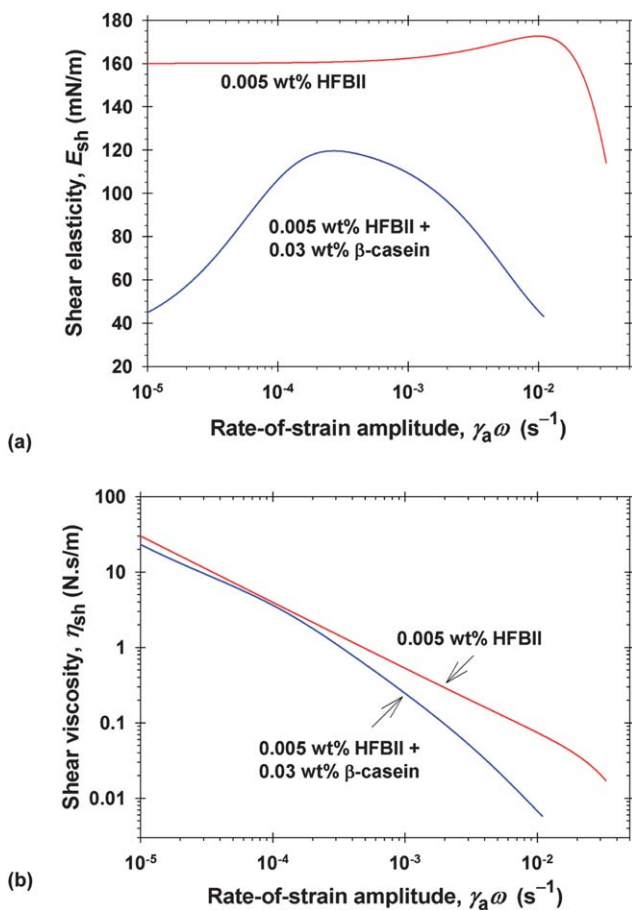


Fig. 12 Comparison of the results for HFBII adsorption layers without and with added β -casein. (a) Surface shear elasticity, E_{sh} , vs. $\gamma_a\omega$ calculated from eqn (27)–(29a) with $\dot{\gamma} \equiv \gamma_a\omega$. (b) Surface shear viscosity, $\eta_{sh} = E_{sh}/\nu_{ch}$, vs. $\gamma_a\omega$, where ν_{ch} is given by eqn (18) with $\dot{\gamma} \equiv \gamma_a\omega$, and with m and Q from Table 3.

(18), is satisfied in the whole region of quasi-linear response of the protein adsorption layers. Moreover, as seen in Fig. 10, the data obtained in the angle-ramp and oscillatory regimes collapse on a single master line, whose slope and intercept determine the parameters m and Q ; see Table 3. The comparison between the two regimes is possible if the data from the oscillatory regime are plotted in terms of average values, $\langle \nu_{ch} \rangle$ vs. $\langle \dot{\gamma} \rangle$ defined by eqn (21) and (24). The full agreement between the data obtained in two very different kinetic regimes confirms the adequacy of the combined Maxwell–Herschel–Bulkley model, which is based on eqn (11), (18) and (19).

In contrast with the dependence $\nu_{ch}(\dot{\gamma})$, the dependence $\eta_{sh}(\dot{\gamma})$, and especially, $E_{sh}(\dot{\gamma})$, can considerably deviate from a power law of Herschel–Bulkley type; see Fig. 11 and 12. The power laws in eqn (17) can be used asymptotically only in the limit of low shear rates; see Fig. 9. Here, the dependence $E_{sh}(\dot{\gamma})$ has been determined by fitting the experimental data with an appropriate empirical curve; see eqn (27) and (29). The dependence $E_{sh}(\gamma_a\omega)$ turns out to be very close to the respective dependence of the average shear elasticity $\langle E_{sh} \rangle$ on the amplitude $\gamma_a\omega$; see Fig. 11. Hence, it is much easier to characterize the dependence of elasticity on the shear rate by

plotting the experimental data as $\langle E_{\text{sh}} \rangle$ vs. $\gamma_a \omega$, where $\langle E_{\text{sh}} \rangle$ is calculated from the experimental G' and G'' using eqn (26), without using any fits, like those in Fig. 11. Data obtained in angle-ramp regime can be added on the same graph by plotting the determined E_{sh} vs. an effective amplitude $\gamma_a \omega \equiv \dot{\gamma}/\mu$. Having once determined E_{sh} , we can further determine the viscosity $\eta_{\text{sh}} = E_{\text{sh}}/\nu_{\text{ch}}$, where ν_{ch} has to be calculated for the same shear rate from eqn (18).

In the framework of the Maxwell model (Fig. 8b), an elastic body corresponds to $E_{\text{sh}} \rightarrow \text{const.}$, $\eta_{\text{sh}} \rightarrow \infty$, and consequently $\nu_{\text{ch}} = E_{\text{sh}}/\eta_{\text{sh}} \rightarrow 0$. In the other limit of a purely viscous body, we have $E_{\text{sh}} \rightarrow \infty$, $\eta_{\text{sh}} \rightarrow \text{const.}$, and consequently $\nu_{\text{ch}} \rightarrow \infty$. Hence, the increase of ν_{ch} indicates fluidization (softening) of the body. In other words, the value of the characteristic frequency, $0 < \nu_{\text{ch}} < \infty$, can serve as an indicator for the degree of fluidization of the viscoelastic protein layer. In this respect, the increase of ν_{ch} with the rate of strain in Fig. 10 indicates fluidization of the adsorption layer upon increasing the shear rate. Likewise, the greater slope of the line in Fig. 10b in comparison with that in Fig. 10a (see the values of m in Table 3) means that the addition of β -casein enhances the softening of the protein layer upon shearing. More detailed information for the viscoelastic behavior of the system can be obtained by calculating separately $\langle E_{\text{sh}} \rangle$ and $\langle \eta_{\text{sh}} \rangle$, as demonstrated above (see Fig. 11 and 12).

Eqn (26) indicates that $\langle E_{\text{sh}} \rangle$ represents a nonlinear combination of the storage and loss moduli G' and G'' . A similar expression holds for the average viscosity

$$\langle \eta_{\text{sh}} \rangle \equiv \frac{\langle E_{\text{sh}} \rangle}{\langle \nu_{\text{ch}} \rangle} = \frac{G'^2 + (m+1)G''^2}{G''\omega} \quad (30)$$

where eqn (21) and (26) have been used. Hence, the popular paradigm that G' and G'' characterize, respectively, the elastic and viscous response of the system (which is correct for the Kelvin model) is not applicable to the investigated viscoelastic protein layers, whose behavior obeys the combined Maxwell–Herschel–Bulkley model. Note that at constant E_{sh} , η_{sh} and $\nu_{\text{ch}} = E_{\text{sh}}/\eta_{\text{sh}}$ [*i.e.* at $m = 0$; see eqn (23)], eqn (26) and (30) transform into eqn (12a). One of the important conclusions from the present study is that if the rheology of the adsorption layer complies with the Maxwell model, then the surface shear viscosity has to be calculated from eqn (30), rather than by the frequently used expression $\eta_{\text{sh}} = G''/\omega$, which corresponds to the Kelvin model. Likewise, if the viscoelastic layer obeys the Maxwell model, then E_{sh} must be estimated from eqn (26), the simple relation $E_{\text{sh}} = G'$ of the Kelvin model being inapplicable.

The data obtained in angle-ramp and oscillatory regimes are mutually complementary. The main advantage of the angle-ramp regime is that it indicates the type of the model, which can provide an adequate description of the system's rheological behavior. In our case, the data obtained in the angle-ramp regime comply with the Maxwell (rather than the Kelvin) model; see Fig. 6 and the related text, as well as preceding studies.^{17,18,36} For protein layers, the main disadvantage of the angle-ramp regime is that the reproducibility of the results is not so high. This demands the measurements to be carried out many times and to take average values. The most probable reason for the lower reproducibility is that the rheology of the protein adsorption layers is sensitive to the surface age, *i.e.* to the prehistory. Conversely, in the oscillatory regime a steady-state periodic strain is imposed, which makes inessential the prehistory of the protein layer. The main advantage of the oscillatory regime is in the enhanced reproducibility of the experimental results. However, in this regime it is difficult to identify the adequate rheological law. A combination of data obtained using the two kinetic regimes allows one to avoid the aforementioned problems.

The Maxwell model, applied to protein adsorption layers, effectively describes the simultaneous stretching, breakage and restoration of intermolecular bonds upon shearing. As seen in Fig. 12a, with the increase of the rate of strain, the elasticity,

E_{sh} , initially increases, reaches a maximum, and then decreases. The initial increase can be interpreted with a predominant effect of stretching, whereas the decrease at higher shear rates—with predominant breakage of intermolecular bonds, which leads to softening of the adsorption layer. It is remarkable that the HFBII layer (without added β -casein) has elasticity which is insensitive to the shear rate in a relatively wide range. The addition of β -casein results in a markedly lower elasticity (Fig. 12a), whereas the viscosity of the β -casein containing layers becomes smaller only at the higher rates of strain (Fig. 12b). These evidences for the intercalation of β -casein molecules in the voids of the HFBII adsorption layer that have been detected by microscopic observations.^{31,45,46} Despite the voids, at the investigated concentrations the HFBII certainly forms an interconnected network at the surface. If this network is broken, then E_{sh} should be considerably lower, as for β -casein alone (see Section 2).

The generalization of the Maxwell model to the case of variable η_{sh} and E_{sh} is nontrivial. The experiment (Fig. 6) indicates that this can be achieved by postulating variable η_{sh} and E_{sh} in eqn (11), which leads to the combined Maxwell–Herschel–Bulkley model, as described above.

A different approach to the generalization of the Maxwell model could be attempted by postulating variable η_{sh} and E_{sh} in eqn (8). In such a case, instead of eqn (11), one obtains:

$$\frac{d}{dt}\left(\frac{\tau_{sh}}{E_{sh}}\right) + \frac{\tau_{sh}}{\eta_{sh}} = \frac{d\gamma}{dt} \quad (31)$$

Because $E_{sh} = E_{sh}(|\dot{\gamma}|)$, eqn (31) leads to the appearance of the derivative

$$\frac{dE_{sh}}{dt} = \frac{dE_{sh}}{d|\dot{\gamma}|} \frac{d|\dot{\gamma}|}{dt} \quad (32)$$

The derivative $d|\dot{\gamma}|/dt$ is a discontinuous function at $\dot{\gamma} = 0$ [we recall that $\dot{\gamma}(t)$ is a sinusoid]. However, the experimental $\tau_{sh}(t)$ dependence is a continuous and smooth function, which means that the postulate used to obtain eqn (31) is in conflict with the experiment.

4.5.2. Comparison of the viscoelastic behavior of different protein adsorption layers. Table 4 shows data for the effect of concentration of added β -casein on the rheological parameters of mixed adsorption layers from solutions containing 0.005 wt% HFBII. The values of m determined from fits like those in Fig. 10 are increasing with the rise of β -casein concentration, which indicates faster fluidization with the rise of the shear rate. The values of $\langle\nu_{ch}\rangle$, $\langle E_{sh}\rangle$ and $\langle\eta_{sh}\rangle$ in Table 4 are calculated from m , G' and G'' by means of eqn (13), (26) and (30) and correspond to amplitude $\gamma_a = 1.74$ mrad and oscillatory frequency $\nu = 1$ Hz. The characteristic

Table 4 Effect of the concentration of added β -casein on the rheological parameters of adsorption layer from a 0.005 wt% HFBII; the values of $\langle\nu_{ch}\rangle$, $\langle E_{sh}\rangle$ and $\langle\eta_{sh}\rangle$ correspond to $\gamma_a = 1.74$ mrad and $\nu = 1$ Hz

β -casein (wt%)	m	$\langle\nu_{ch}\rangle$ (s ⁻¹)	$\langle E_{sh}\rangle$ (mN m ⁻¹)	$\langle\eta_{sh}\rangle$ (N.s/m)
0.015	0.81	1.10	133	0.110
0.030	0.82	1.16	111	0.082
0.045	0.91	1.23	124	0.101
0.070	0.98	2.06	79.5	0.039

frequency $\langle \nu_{\text{ch}} \rangle$ increases with the rise of β -casein concentration. In addition, $\langle E_{\text{sh}} \rangle$ and $\langle \eta_{\text{sh}} \rangle$ exhibit a tendency to decrease (excluding the point at 0.045 wt% HFBII). In general, the data in Table 4 indicate an increasing fluidization (softening) of the mixed protein adsorption layer with the rise of the β -casein concentration.

The difference between the values of m at 0.030 wt% β -casein concentration in Tables 3 and 4 is due to the fact that the data in Table 4 have been obtained with another sample of β -casein, the one that was used in ref. 36.

For HFBII, G' is ca 10 and 100 times greater than for BLG and β -casein, respectively.¹¹ However, the difference between the values of $\langle \nu_{\text{ch}} \rangle$ in Fig. 10c is not so great, especially for BLG and HFBII. This is due to the fact that $\langle \nu_{\text{ch}} \rangle = \langle E_{\text{sh}} \rangle / \langle \eta_{\text{sh}} \rangle$, and the softening of the adsorption layer may lead to a decrease of both $\langle E_{\text{sh}} \rangle$ and $\langle \eta_{\text{sh}} \rangle$, so that the changes in their ratio $\langle \nu_{\text{ch}} \rangle$ can be not so significant. For this reason, the viscoelastic properties of protein adsorption layers should be characterized by the dependencies of two parameters, *e.g.* $\langle \nu_{\text{ch}} \rangle$ and $\langle E_{\text{sh}} \rangle$, on the shear rate.

Our experiments have been carried out at a fixed temperature, 25 °C. The investigation of the temperature dependence of $\langle \nu_{\text{ch}} \rangle$, $\langle E_{\text{sh}} \rangle$ and $\langle \eta_{\text{sh}} \rangle$ can be a subject of a subsequent study. If the increase of temperature also leads to softening of the adsorption layers, then the strain rate could be interpreted as an effective temperature, as in the studies on concentrated particle suspensions (colloidal glasses).^{47,48}

4.5.3. Applications to long-term foam stability. The experiment shows that the main reason for the decay of foams formed from protein solutions is the phenomenon foam disproportionation (Ostwald ripening).^{49,50} This phenomenon is related to the transfer of gas across the foam films from the smaller to the bigger bubbles driven by the higher pressure in the smaller bubbles. As a result, the smaller bubbles shrink and disappear, whereas the bigger bubbles grow. This process can be characterized by the rate of decrease of the volume V of a small bubble:⁵¹

$$-\frac{dV}{dt} = k_g A \frac{p_c}{p_a} \approx k_g A \frac{1}{p_a} \frac{2\sigma}{R} \quad (33)$$

where t is time, A is the film area, $p_a = \text{const.}$ is the atmospheric pressure; $p_c \approx 2\sigma/R$ is the capillary pressure with σ being the surface tension; R is the bubble radius, and k_g is the permeability of the film to gas. Dense viscoelastic protein adsorption layers on the bubble surfaces can suppress the foam disproportionation in two ways: (i) decrease of the surface tension, σ , and (ii) decrease of the permeability k_g ; see eqn (33). Indeed, upon the bubble shrinking the protein layer on its surface is spontaneously compressed and solidifies, and can have a very low surface tension, which is evidenced by the appearance of wrinkles on the bubble surface.^{9,52} Second, the solidification of the protein adsorption layer can lead to a significant decrease of the permeability of the foam films to gases, k_g . The main reason for that is the low solubility and diffusivity of the gas molecules in the respective condensed adsorption layer, which has solid rather than fluid molecular packing.⁵⁰ In this respect, better foam-stabilizing effect is expected from adsorption monolayers of higher E_{sh} and lower ν_{ch} that indicate a higher rigidity of the film.

Experimentally, solidification phase transition of a HFBII adsorption layer was detected upon increase of the surface pressure π_s (and surface coverage) by means of the pendant-drop method.⁵³ At 25 °C, the transition occurs at $\pi_s \approx 22 \text{ mN m}^{-1}$. It is registered by the sharp increase of the error of the fit of the pendant-drop profile by the Laplace equation of capillarity. This effect is explained with the fact that the solidified protein adsorption layer has an anisotropic tensorial surface tension, whereas the Laplace equation presumes isotropic surface tension.^{52,54} The same method⁵³ could be applied to investigate the temperature dependence of the solidification phase transition for adsorption layers of various proteins.

5.1. Effects of the frequency and strain amplitude

Here, our goal is to investigate the behavior of the protein adsorption layers at higher values of the rate of strain $\dot{\gamma} = \gamma_a \omega \cos(\omega t)$. The amplitude $\gamma_a \omega$ can be increased by raising either the strain γ_a , or the angular frequency $\omega = 2\pi\nu$. Fig. 13a and b show plots of the experimental data for the stress $\tau_{sh}(t)$ vs. strain $\gamma(t)$ (Lissajous plot) corresponding to the same frequency, $\nu = 1$ Hz, but to two different strain amplitudes: $\gamma_a = 1.05$ and 2.10%. The respective rate-of-strain amplitudes are $\gamma_a \omega = 0.066$ and 0.132 s^{-1} . The non-elliptical (parallelogram-shaped) Lissajous curves in Fig. 13a and b indicate that the rheological response of the layer is nonlinear (see Section 3.1 above).

Fig. 13c shows a similar Lissajous plot of the experimental data from Fig. 2b obtained at a higher frequency, $\nu = 4$ Hz, but at a lower strain amplitude, $\gamma_a = 0.174\%$, so that the rate-of-strain amplitude is $\gamma_a \omega = 0.044 \text{ s}^{-1}$, *i.e.* it is smaller than those corresponding to Fig. 13a and b. The scattered points in Fig. 13c (the lack of Lissajous curve) imply that there is no definite relation between the stress and strain in this specific case. This could be interpreted as breakage of the elastic network formed by the adsorbed hydrophobin molecules at the air/water interface. The solid line (the ellipse) in Fig. 13c represents the sinusoid that is drawn as fit of the data in Fig. 2b. The comparison of the three plots in Fig. 13 indicates that at comparable rates of strain the increase of the frequency ω damages the viscoelastic adsorption layer easier than the increase of the strain amplitude, γ_a .

5.2. Fits of the Lissajous curves with the theoretical model

Here, our aim is to demonstrate that the combined Maxwell–Herschel–Bulkley model, based on eqn (11) and (18) can provide a quantitative description of the experimental Lissajous curves in the case of nonlinear response, as in Fig. 13a and b.

In the case of nonlinear response, the use of Fourier expansions, like eqn (6), is not convenient, because of the appearance of two infinite series of coefficients, G'_k and G''_k , $k = 1, 3, 5, \dots$. Instead, we could integrate the basic equation of the Maxwell model, eqn (11). Substituting $\dot{\gamma} = \gamma_a \omega \cos(\omega t)$, we bring eqn (11) in the form:

$$\frac{d\tau_{sh}}{d\xi} + \frac{\nu_{ch}}{\omega} \tau_{sh} = E_{sh} \gamma_a \cos \xi \quad (34)$$

where $\xi \equiv \omega t$. Applying the known formula for the solution of a linear first-order differential equation, from eqn (34) we obtain:

$$\tau_{sh}(\xi) = f(\xi) \left[\tau_{sh}(0) + \gamma_a \int_0^{\xi} \frac{E_{sh}(\hat{\xi})}{f(\hat{\xi})} \cos \hat{\xi} d\hat{\xi} \right] \quad (35)$$

$$\text{where } f(\xi) \equiv \exp \left[- \int_0^{\xi} \frac{\nu_{ch}(\hat{\xi})}{\omega} d\hat{\xi} \right] \quad (36)$$

$\hat{\xi}$ and $\tau_{sh}(0)$ are, respectively, integration variable and constant. For a periodic variation of the stress, we have $\tau_{sh}(0) = \tau_{sh}(2\pi)$. Then, eqn (35) gives an expression for determining the integration constant:

$$\tau_{sh}(0) = \frac{\gamma_a f(2\pi)}{1 - f(2\pi)} \int_0^{2\pi} \frac{E_{sh}(\xi)}{f(\xi)} \cos \xi d\xi \quad (37)$$

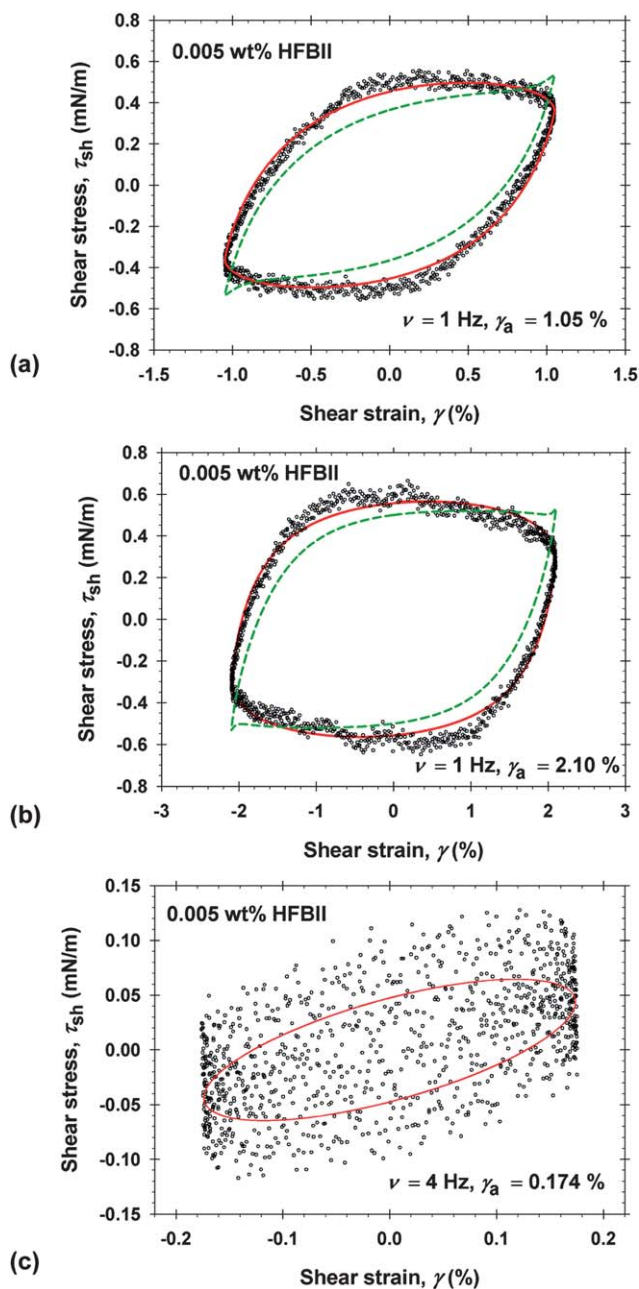


Fig. 13 Lissajous plots of experimental data for the stress vs. strain. The dashed lines are drawn using m , Q and $E_{sh}(\dot{\gamma})$ determined in quasi-linear regime (section 4). The solid lines are fits by means of eqn (35)–(37) using m , Q and E_{sh} as adjustable parameters. (a) Data from Fig. 3a for $\nu = 1$ Hz and $\gamma_a = 1.05\%$; (b) Data from Fig. 3b for $\nu = 1$ Hz and $\gamma_a = 2.10\%$. (c) Data from Fig. 2b for $\nu = 4$ Hz and $\gamma_a = 0.174\%$; in this special case the solid line represents the sinusoidal fit in Fig. 2b.

Table 5 Comparison of parameters determined from the fits of data in Fig. 13a and b (0.005 wt % Online % HFBII, nonlinear response) with the respective values for quasi-linear response (the first line)

$\gamma_a\omega$ (s ⁻¹)	m	Q (s ^{$m-1$})	E_{sh} (mN m ⁻¹)	$\langle\nu_{ch}\rangle$ (Hz)	$\langle\eta_{sh}\rangle$ (mN.s/m)
<0.033	0.88	134	≥ 133	≤ 3.06	≥ 17.3
0.066	0.58	83	137	9.81	14.0
0.132	0.45	80	137	20.5	6.7

The dashed lines in Fig. 13a and b are calculated from eqn (35)–(37) using m , Q and $E_{sh}(\dot{\gamma})$ determined in quasi-linear regime (Section 4). In particular, ν_{ch} is calculated from eqn (18) with m and Q from Table 3. In addition, E_{sh} is calculated from eqn (27) and (28) with $\dot{\gamma} = \gamma_a\omega \cos\xi$. As seen on Fig. 13a and b, the theoretical curves calculated in this way do not agree with the experimental data.

To fit the data in Fig. 13a and 13b, we calculated τ_{sh} from eqn (35)–(37) using m , Q and E_{sh} as adjustable parameters. In particular, $\nu_{ch}(\xi)$ was calculated from the modified Herschel–Bulkley law, eqn (18) with $\dot{\gamma} = \gamma_a\omega \cos\xi$. For $E_{sh}(\xi)$ we cannot use the empirical expression, eqn (27), because it has been obtained as a fit at lower shear rates. Unlike the viscosity η_{sh} , the elasticity E_{sh} is not varying too much, so that a reasonable approximation is to substitute $E_{sh} = \text{const.}$ in eqn (35) and (37) and to determine its value as an adjustable parameter (an averaged elasticity) from the fit. The best fits are shown by solid lines in the respective figures, and the obtained parameters are given in Table 5. It is curious that the same values of E_{sh} were obtained from the fits of the data corresponding to the two different γ_a . Furthermore, substituting the obtained m and Q in eqn (23)–(24), we obtain $\langle\nu_{ch}\rangle$. Finally, the averaged viscosity is calculated from the expression $\langle\eta_{sh}\rangle = E_{sh}/\langle\nu_{ch}\rangle$. The obtained values are given in Table 5.

The first line of Table 5 shows parameter values corresponding to quasi-linear response; the maximal value of $\langle\nu_{ch}\rangle$ (from Fig. 10a) and the minimal values of of E_{sh} and η_{sh} (from Fig. 11a) are given for comparison. The last two lines of Table 5 show the parameters corresponding to the fits of the data in Fig. 13a and b. The results show that $\langle\nu_{ch}\rangle$ increases with the rise of the rate-of-strain amplitude $\gamma_a\omega$, which indicates an increasing fluidization of the adsorption layer (see Section 4.5). In addition, the last column of Table 5 indicates shear thinning, as it should be expected.

Fig. 14 compares the values of m and Q in the cases of quasi-linear and nonlinear rheological response of the HFBII adsorption layer. In the case of quasi-linear response, the values of m and Q are constant, independent of the rate-of-strain amplitude, $\gamma_a\omega$. In the case of nonlinear response, both m and Q are decreasing with $\gamma_a\omega$. This could be explained with structural changes in the adsorption layer that appear at rate-of-strain amplitudes $\gamma_a\omega > 0.033$ s⁻¹. In Fig. 13c, the lack of a definite stress-vs.-strain dependence indicates that at higher frequencies the viscoelastic network of interconnected protein molecules at the interface can be destroyed.

In conclusion, the application of the combined Maxwell–Herschel–Bulkley model to the case of nonlinear response allows one to determine the elasticity and viscosity of the layer (Table 5) by fitting the Lissajous curves (Fig. 13a and b) with eqn (35)–(37). In this case the parameters m and Q of the modified Herschel–Bulkley law depend on the rate-of-strain amplitude, which indicates structural changes in the adsorption layer that precede its breakage. So, our recommendation is the comparison of different protein adsorption layers to be carried out in the regime of quasi-linear response, where the layer behaves as a viscoelastic body characterized by constant rheological parameters Q and m in a relatively wide range of shear-rate amplitudes; see Fig. 10 and 14.

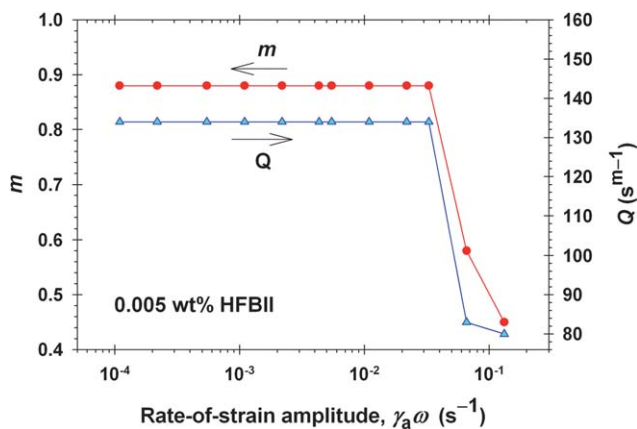


Fig. 14 Plots of m and Q from Table 5 vs. the experimental rate-of-strain amplitude. These two parameters are constant in the region of quasi-linear response (the line in Fig. 10a), but both of them decrease in the region of nonlinear response (Fig. 13a and b).

6. Conclusions

A rheological model of viscoelastic protein adsorption layers is developed, which allows one to determine the interfacial shear elasticity and viscosity, E_{sh} and η_{sh} , as universal functions of the shear rate $\dot{\gamma}$, which are the same irrespective of the used kinetic regime: angle ramp or oscillations. In general, experiments in different regimes give different values of E_{sh} and η_{sh} , but the present analysis shows that the obtained experimental points must lay on universal curves $E_{sh}(\dot{\gamma})$ and $\eta_{sh}(\dot{\gamma})$. Experimental stress-vs.-strain dependences were obtained for adsorption layers of the protein hydrophobin HFBII and its mixture with β -casein. These protein layers exhibit a well pronounced viscoelastic behavior, which is usually characterized by the phenomenological storage and loss moduli, G' and G'' .⁹⁻¹¹ These moduli depend on two kinetic parameters, frequency and amplitude of oscillations, and it has been unclear how they are related to the true surface shear elasticity and viscosity. Our analysis of data in both angle-ramp and oscillatory regimes revealed that the rheological behavior of the system obeys a combined Maxwell–Herschel–Bulkley model. In the angle-ramp regime, the fits of the experimental rheological curves give directly E_{sh} and η_{sh} . Their ratio, $\nu_{ch} = E_{sh}/\eta_{sh}$, represents a characteristic frequency of the system's rheological response. In oscillatory regime, these three quantities are universal functions of the rate of strain: $E_{sh}(\dot{\gamma})$, $\eta_{sh}(\dot{\gamma})$ and $\nu_{ch}(\dot{\gamma})$. Because the latter functions exhibit periodic variations, the comparison with the angle-ramp regime has to be made in terms of the average values of the respective quantities, $\langle E_{sh} \rangle$, $\langle \eta_{sh} \rangle$ and $\langle \nu_{ch} \rangle$, defined as described in the text. A complete agreement between the results obtained in the two different kinetic regimes has been achieved. It turns out, that only $\langle \nu_{ch} \rangle$ obeys a simple law of Herschel–Bulkley type, $\langle \nu_{ch} \rangle = Q \langle \dot{\gamma} \rangle^m$, in a wide range—more than three orders of magnitude; see Fig. 10. The dependences $E_{sh}(\dot{\gamma})$ and $\eta_{sh}(\dot{\gamma})$ are more complex than the simple Herschel–Bulkley power law for $\langle \nu_{ch} \rangle$. The determination of the basic rheological parameters Q and m allows comparison of different viscoelastic protein layers. Q and m can be determined from the experimental data for the moduli G' and G'' , and subsequently, $E_{sh}(\dot{\gamma})$ and $\eta_{sh}(\dot{\gamma})$, and their average values, $\langle E_{sh} \rangle$ and $\langle \eta_{sh} \rangle$, can be calculated. The characteristic frequency ν_{ch} plays a central role in the rheological model. Its value, $0 < \nu_{ch} < \infty$, characterizes the softness/rigidity of the medium ($0 =$ elastic layer; $\infty =$ viscous fluid layer). Despite the nonlinear character of the Herschel–Bulkley law, the protein adsorption layers exhibit a quasi-linear rheological response in a wide range of shear-rate amplitudes. However, at greater amplitudes nonlinear effects appear, which are detected

by the presence of a non-negligible third harmonic in the Fourier expansion of $\tau_{sh}(\dot{\gamma})$ and by a non-elliptic (parallelogram shaped) Lissajous plot. The combined Maxwell–Herschel–Bulkley model can be applied also to the regime of nonlinear response, but in this case the parameters Q and m become dependent on the rate-of-strain amplitude. In general, the nonlinear rheological response indicates structural changes in the protein adsorption layer caused by the more intensive shearing, which leads to breakage of the interfacial viscoelastic network at sufficiently high frequencies. For this reason, it is recommended to investigate the rheology of protein adsorption layer in the regime of quasi-linear response, for which the layer is characterized with constant Q and m , as well as with representative $E_{sh}(\dot{\gamma})$ and $\eta_{sh}(\dot{\gamma})$ dependencies. The results can be utilized for the optimization and control of the properties of fluid dispersions stabilized by protein adsorption layers. From a formal viewpoint, the developed approach can be applied to any viscoelastic continuum, not necessarily a protein layer.

Acknowledgements

The authors gratefully acknowledge the support from Unilever Research; from the National Science Fund of Bulgaria, grant No. DO-02-121/2009, and from ESF COST Action CM1101. The authors are grateful to Ms. Mariana Paraskova for her assistance in figure preparation.

References

- 1 A. J. Wilson, in *Foams*, ed. R. K. Prud'homme and S. A. Khan, Marcel Dekker, New York, 1996, ch. 5, pp. 243–285.
- 2 K. Mysels, K. Shinoda and S. Frankel, *Soap Films*, Pergamon, London, 1959.
- 3 D. A. Edwards, H. Brenner and D. T. Wasan, *Interfacial Transport Processes and Rheology*, Butterworth-Heinemann, Boston, 1991.
- 4 I. B. Ivanov, K. D. Danov and P. A. Kralchevsky, *Colloids Surf., A*, 1999, **152**, 161–182.
- 5 S. A. Koehler, S. Hilgenfeldt and H. A. Stone, *Langmuir*, 2000, **16**, 6327–6341.
- 6 K. Golemanov, S. Tcholakova, N. D. Denkov, K. P. Ananthapadmanabhan and A. Lips, *Phys. Rev. E: Stat., Nonlinear, Soft Matter Phys.*, 2008, **78**, 051405.
- 7 K. Tsujii, *Surface Activity: Principles, Phenomena and Applications*, Academic Press, London, 1998.
- 8 W. Xu, A. Nikolov, D. T. Wasan, A. Gonsalves and R. P. Borwankar, *Colloids Surf., A*, 2003, **214**, 13–21.
- 9 A. R. Cox, F. Cagnol, A. B. Russell and M. J. Izzard, *Langmuir*, 2007, **23**, 7995–8002.
- 10 A. R. Cox, D. L. Aldred and A. B. Russell, *Food Hydrocolloids*, 2009, **23**, 366–376.
- 11 T. B. J. Blijdenstein, P. W. N. de Groot and S. D. Stoyanov, *Soft Matter*, 2010, **6**, 1799–1808.
- 12 D. E. Graham and M. C. Phillips, *J. Colloid Interface Sci.*, 1980, **76**, 240–250.
- 13 E. Dickinson, B. S. Murray and G. Stainsby, *J. Colloid Interface Sci.*, 1985, **106**, 259–262.
- 14 D. Langevin, *Adv. Colloid Interface Sci.*, 2000, **88**, 209–222.
- 15 R. Borbas, B. S. Murray and E. Kiss, *Colloids Surf., A*, 2003, **213**, 93–103.
- 16 E. M. Freer, K. S. Yim, G. G. Fuller and C. J. Radke, *Langmuir*, 2004, **20**, 10159–10167.
- 17 I. Panaiotov, D. S. Dimitrov and L. Ter-Minassian-Saraga, *J. Colloid Interface Sci.*, 1979, **72**, 49–53.
- 18 P. M. Vassilev, S. Taneva, I. Panaiotov and G. Georgiev, *J. Colloid Interface Sci.*, 1981, **84**, 169–174.
- 19 J. Krägel, R. Wüstneck, D. Clark, P. Wilde and R. Miller, *Colloids Surf., A*, 1995, **98**, 127–135.
- 20 S. Roth, B. S. Murray and E. Dickinson, *J. Agric. Food Chem.*, 2000, **48**, 1491–1497.
- 21 J. Krägel, S. R. Derkach and R. Miller, *Adv. Colloid Interface Sci.*, 2008, **144**, 38–53.
- 22 B. S. Murray and E. Dickinson, *Food Sci. Technol.*, 1996, **2**, 131–145.
- 23 R. Miller, R. Wüstneck, J. Krägel and G. Kretzschmar, *Colloids Surf., A*, 1996, **111**, 75–118.
- 24 E. Dickinson, *Colloids Surf., B*, 2001, **20**, 197–210.
- 25 M. A. Bos and T. van Vliet, *Adv. Colloid Interface Sci.*, 2001, **91**, 437–471.
- 26 J. Krägel and S. R. Derkach, *Curr. Opin. Colloid Interface Sci.*, 2010, **15**, 246–255.
- 27 R. Miller, J. K. Ferri, A. Javadi, J. Krägel, N. Mucic and R. Wüstneck, *Colloid Polym. Sci.*, 2010, **288**, 937–950.

- 28 M. Reger, T. Sekine, T. Okamoto and H. Hoffmann, *Soft Matter*, 2011, **7**, 8248–8257. [View Online](#)
- 29 M. Reger, T. Sekine, T. Okamoto, K. Watanabe and H. Hoffmann, *Soft Matter*, 2011, **7**, 11021–11030.
- 30 B. Niu, D. Wang, Y. Yang, H. Xu and M. Qiao, *Amino Acids*, 2012, **42**, DOI: 10.1007/s00726-011-1126-5.
- 31 M. B. Linder, *Curr. Opin. Colloid Interface Sci.*, 2009, **14**, 356–363.
- 32 J. Hakanpää, A. Paananen, S. Askolin, T. Nakari-Setälä, T. Parkkinen, M. Penttilä, M. B. Linder and J. Rouvinen, *J. Biol. Chem.*, 2004, **279**, 534–539.
- 33 E. S. Basheva, P. A. Kralchevsky, N. C. Christov, K. D. Danov, S. D. Stoyanov, T. B. J. Blijdenstein, H.-J. Kim, E. G. Pelan and A. Lips, *Langmuir*, 2011, **27**, 2382–2392.
- 34 E. S. Basheva, P. A. Kralchevsky, K. D. Danov, S. D. Stoyanov, T. B. J. Blijdenstein, E. G. Pelan and A. Lips, *Langmuir*, 2011, **27**, 4481–4488.
- 35 X. L. Zhang, J. Penfold, R. K. Thomas, I. M. Tucker, J. T. Petkov, J. Bent, A. Cox and R. A. Campbell, *Langmuir*, 2011, **27**, 11316–11323.
- 36 G. M. Radulova, K. Golemanov, K. D. Danov, P. A. Kralchevsky, S. D. Stoyanov, L. N. Arnaudov, E. G. Pelan and A. Lips, *Langmuir*, 2012, **28**, 4168–4177.
- 37 G. B. Bantchev and D. K. Schwartz, *Langmuir*, 2003, **19**, 2673–2682.
- 38 M. H. Lee, D. H. Reich, K. J. Stebe and R. L. Leheny, *Langmuir*, 2010, **26**, 2650–2658.
- 39 P. Erni, P. Fischer, E. J. Windhab, V. Kusnezov, H. Stettin and J. Läger, *Rev. Sci. Instrum.*, 2003, **74**, 4916–4924.
- 40 K. Hyun, M. Wilhelm, C. O. Klein, K. S. Cho, J. G. Nam, K. H. Ahn, S. J. Lee, R. H. Ewoldt and G. H. McKinley, *Prog. Polym. Sci.*, 2011, **36**, 1697–1753.
- 41 W. Thomson, *Proc. R. Soc. London*, 1865, **14**, 289–297, DOI: 10.1098/rspl.1865.0052.
- 42 W. Voigt, *Ann. Phys. Chem.*, 1892, **283**, 671–693, DOI: 10.1002/andp.18922831210.
- 43 J. C. Maxwell, *Philos. Trans. R. Soc. London*, 1867, **157**, 49–88; URL: <http://www.jstor.org/stable/108968>.
- 44 W. H. Herschel and R. Bulkeley, *Kolloid-Z.*, 1926, **39**, 291–300, DOI: 10.1007/BF01432034.
- 45 A. Paananen, E. Vuorimaa, M. Torkkeli, M. Penttilä, M. Kauranen, O. Ikkala, H. Lemmetyinen, R. Serimaa and M. B. Linder, *Biochemistry*, 2003, **42**, 5253–5258.
- 46 G. R. Szilvay, A. Paananen, K. Laurikainen, E. Vuorimaa, H. Lemmetyinen, J. Peltonen and M. B. Linder, *Biochemistry*, 2007, **46**, 2345–2354.
- 47 C. Eisenmann, C. Kim, J. Mattsson and D. A. Weitz, *Phys. Rev. Lett.*, 2010, **104**, 035502.
- 48 H. M. Vollebregt, R. G. M. van der Sman and R. M. Boom, *Soft Matter*, 2010, **6**, 6052–6064.
- 49 D. J. Carp, J. Wagner, G. B. Bartholomai and A. M. R. Pilosof, *J. Food Sci.*, 1997, **62**, 1105–1109.
- 50 S. Tcholakova, Z. Mitrinova, K. Golemanov, N. D. Denkov, M. Vethamuthu and K. P. Ananthapadmanabhan, *Langmuir*, 2011, **27**, 14807–14819.
- 51 H. M. Princen and S. G. Mason, *J. Colloid Sci.*, 1965, **20**, 353–375.
- 52 K. D. Danov, P. A. Kralchevsky and S. D. Stoyanov, *Langmuir*, 2010, **26**, 143–155.
- 53 N. A. Alexandrov, K. G. Marinova, T. D. Gurkov, K. D. Danov, P. A. Kralchevsky, S. D. Stoyanov, T. B. J. Blijdenstein, L. N. Arnaudov, E. G. Pelan and A. Lips, *J. Colloid Interface Sci.*, 2012, **376**, 296–306.
- 54 J. T. Petkov, T. D. Gurkov, B. E. Campbell and R. P. Borwankar, *Langmuir*, 2000, **16**, 3703–3711.